Measuring Magnetic Field Gradients using Electromagnetically Induced Transparency in Rb Vapor

A thesis submitted in partial fulfillment of the requirement
for the degree of Bachelor of Science with Honors in
Physics from the College of William and Mary in Virginia,

by

Ravn M. Jenkins

Accepted for Honors

Advisor: Prof. Irina Novikova

Prof. Eugeniy Mikhailov

Seth Aubin

Prof. Seth Aubin

Prof. Nahum Zobin

Williamsburg, Virginia
May 2019

Contents

Acknowledgments iii

List of Figures vii

List of Tables v

1 Introduction 1

2 Theory 3

2.1 Electromagnetically Induced Transparency 3

2.2 Atomic Energy Levels and the Zeeman Effect 4

2.3 Benefits of the dual-rail configuration 5

3 Methods 8

3.1 Experimental Design 8

3.2 Magnetic Field Generation 9

3.3 Magnetic Field Calibration 13

3.3.1 Solenoid Calibration 13

3.3.2 Calibrating Single Wire Gradient 14

3.3.3 Gradient Coil Calibration 15

4 Constant Gradients 17

4.1 Straight-wire Gradient Measurement 17

4.2 Linear Gradient Coil Measurements 18

5 AC Gradients 20

5.1 Lock-in Amplifier Optimization 21

5.2 Power Optimization 24

5.3 Measuring AC Gradients 24

6 Conclusions and Future Work 26

6.1 Atomic Density Calibration 28

6.2 Transit Ramsey EIT resonances 30

Acknowledgments

I would first and foremost like to thank my parents and grandparents for their endless support of my education. I am also deeply grateful to my advisers, Irina and Eugeniy, for introducing me to the wonderful world of optics. Thanks to Hana Warner and Kangning Yang for their help with the initial experiment construction, as well as to Alex Fay for the gradient coil construction. I would like to acknowledge the support of the DeWilde research fellowship and the National Science Foundation grant PHY308281.

List of Figures

2.1 (a) Example of a three-level Λ configuration. (b) An EIT resonance. Modified from Ref [5] 4

2.2 (a) Level diagram for D1 line of Rb showing the Zeeman sublevels. (b) Coherent population trapping resonance at zero magnetic field and for B = 16μT, B=35μT. Modified from Ref [5] 5

2.3 (a) Simulated single-channel signals with a slight offset, (b) resulting differential signal 6

2.4 (a)The channel 1, channel 2, and differential signals of the m=-2 resonance. (b) Comparison of subtracting individual channels recorded separately vs the differential signal 6

3.1 Setup schematic for differential detection.PBS=polarizing beam splitter, HWP=half wave plate, QWP=quarter wave plate WP= Wollaston Prism, PD=photodiode. 9

3.2 (a) Raw EIT single-channel transmission peak (b) EIT single-channel transmission peak after processing of the lock-in amplifier. 10

3.3 Methods for generating magnetic fields around the R^{87} cell (a) A constant longitudinal magnetic field is created by a solenoid. (b) the single-wire gradient configuration. (c) The two-wire gradient configuration. 10

3.4 (a) Differential signal for various gradient currents (b) Analyzing signal size (depth) vs current. 11

3.5 Gradient coil. The cell of ^{87}Rb vapor will be suspended inside the gradient coil, which in turn is inside the solenoid. 12

3.6 Calibrating the solenoid of the second cell. (a) Resonance width vs solenoid current for Δm=0,2 (b)Plotting single channel resonance position versus current. 13

3.7 Front wire gradient calibration. (a) Single-channel signal for various currents. (b) Single-channel splitting vs current 14

3.8 Linear gradient coil calibration. (a)Frequency separation vs voltage applied to gradient coil. (b) Magnetic field vs voltage applied to gradient coil. 16

4.1 (a) Differential Signal for small currents (b) Analyzing signal height and depth vs current. 18

4.2 (a)Differential signal of the Δ m=-2 resonance with a 35μT Earth-like magnetic field and 0, 9, and 30nT/cm gradients applied. (b) Subtracting the 0-gradient signal from differential signal. (c) Differential signal height vs gradient. 19

5.1 a) Lock-in amplifier output with a 1Hz sine wave with an amplitude of 40 mV applied to the linear gradient coil. b) Zoom in on 60-80 second range to see short term oscillation. 20

5.2 a) Fourier transform of lock-in amplifier output with 1Hz sine wave with an amplitude of 0, 10, and 40 mV applied to the linear gradient coil. Note peak at 1 Hz and 60Hz. b) Zoom in on 1Hz peak, which shows dependence on sine wave amplitude. 21

5.3 Alan variance vs time for a variety of time constants (τ_{mod}). "Dark" signifies that the laser beams were blocked while taking that data. . . 22
5.4 Optimizing Modulation Frequency. a) Gradients on, 1 Hz peak for various applied modulation frequencies. b) Gradients off, noise near 1Hz for various modulation frequencies. c) Signal-to-noise ratio vs modulation frequency. Optimal modulation frequency: 17kHz 23
5.5 (a) Signal-to-noise ratio vs modulation amplitude. Optimal modulation amplitude: 0.22V (b) Signal-to-noise ratio vs modulation gain. Optimal modulation gain: 10mV 23
5.6 Signal-to-noise ratio versus laser beam power 24
5.7 (a) Height of the lock-in amplifier's Fourier-transform 1Hz peak vs gradient. Noise floor indicates minimum peak size that can be discerned above noise. (b) Zooming in on crossing of noise floor gives the sensitivity, 50μT/cm 25

6.1 Example of ^{87}Rb Absorption Spectrum at 57 C 29
6.2 Setup schematic for differential detection. For single channel measurement one of the channels is blocked before the cell. (a) Beam is split using beam splitter and mirror. (b) Setup with delay stage for TREIT work. 30
6.3 (a) Non-zero differential signal with 0 applied magnetic fields (first observation of TREIT resonance)(b) The differential lock-in signals as a function of the two-photon detuning for different relative prism position. Laser power in each channel is 50 μ W. (c) Theoretical simulations of the lock-in readout of the differential TREIT. 6b and 6c modified from Ref [7] 31

6.4 (a)Examples of the optical transmission for a single-channel EIT and for the intensity difference between the two channels. (b) Simplified geometry of the two-channel transient EIT setup. The arrows in the circles indicate the dark state phases of two atoms traveling symmetrically between the beams. For this illustration we set the phase between the two EIT optical fields to be zero in the first beam and ϕ HF $\neq 0$ for the second beam. In case of the non-zero two-photon detuning δ, the dark state phases of both atoms evolve by $\phi\delta = \delta \cdot \tau$ after τ transit time between the two beams, resulting in the difference in the optical response during the repeated interrogation. (c) (i) Slope of the error lock-in signal for each optical channel and for the differential signal at the corresponding zero-crossing detunings. (ii) lock-in noise measured at zero-crossing two-photon position. Horizontal line shows the dark electronic noise level. (iii) Signal-to-noise ratio (defined as slope of the error signal divided by the measure noise). For the differential measurements the average power between the two channel is used. Modified from Ref [7] 32

List of Tables

5.1 Optimized lock-in settings 24

6.1 Cell temperature vs ^{87}Rb density 28

Abstract

We demonstrate a new method for measuring magnetic gradients in the presence of large constant magnetic fields using electromagnetically induced transparency in rubidium vapor. As the Earth provides a near-constant magnetic field of 25-50 μT, most measurements of small magnetic fields involve subtracting or shielding the Earth's field. Our method can measure small gradients in the presence of large magnetic fields using Electromagnetically Induced Transparency in ^{87}Rb. By comparing the resonances of two laser beams in a dual-rail arrangement propagating through rubidium vapor in a spatially changing magnetic field, we are able to measure a constant gradient of $\geq$7 nT/cm and a time-varying gradient of $\geq$50 pT/cm, over a constant magnetic field of 35μT.

Chapter 1

Introduction

Modern magnetometers can accurately measure small magnetic fields, for example the commercial superconducting quantum interface device (SQUID) can measure the magnitude of magnetic fields to 1 fT [1], while the spin exhange relaxation free magnetometer (SERF) has a sensitivity on the order of 1 attoTesla [2]. The challenge remains, however, in measuring small changes to a large external magnetic field. Furthermore, SQUID devices are expensive and require cryogenic temperatures. An inexpensive magnetometer that can measure small magnetic fields without shielding or cooling would have applications in geological and archaeological surveys, defense, space science, and medicine. We are particularly interested in developing a magnetic field gradiometer that can be used in magnetocardiology, a diagnostic procedure which measures the magnetic fields produced by the electric currents in the human heart [3]. These magnetocardiograms require a sensitivity of 10-50 pT [4]

Atomic magnetometers measure magnetic fields using the Zeeman effect, or the splitting of an atom's degenerate energy levels when exposed to an external magnetic field. This splitting causes the atom's absorption resonances to shift in frequency. We can record that splitting using the Electromagnetically Induced Transparency (EIT) transmission peak, and thus measure the magnitude of the external magnetic field. EIT creates a narrow transparent "window" in an absorption line of atoms in a lambda configuration, as the atoms enter a superposition of ground states. As the width of the transmission peak is narrow ($<$ 1MHz) compared to the width of the Doppler-broadened atomic absorption line (500 MHz), studying this peak allows us to measure the degenerate level splitting, and thus the magnetic field, to a much higher accuracy. To measure a magnetic gradient, we propagate two beams through Rb vapor to which a magnetic gradient is applied. As each beam is propagating through a region of slightly different magnetic field magnitude, comparing the EIT resonance position for both beams allows us to measure the gradient of the field. To do this, we use a balanced photodiode to subtract one EIT resonance from the other, and analyze the resulting differential signal. Using the differential signal also removes common noise.

We are interested in measuring both constant magnetic field gradients and magnetic field gradients that change periodically over time (referred to as AC gradients). As measuring either type of gradient required different types of optimization and data analysis, our work involving constant gradients and AC gradients is separated into two chapters. We demonstrate a technique that can measure an alternating gradient (generated by a 1 Hz sine wave) of 50 pT/cm and a constant gradient of 7nT/cm over an earth-like magnetic field of 35 μT.

Some work on this project was completed in the summer of 2018 with the help of a Dewilde Research Fellowship. The description of my summer work is found in Appendix B. It details my exploration of Transit Ramsey EIT Resonances, a phenomenon we encountered that must be accounted for in a dual-rail experiment using EIT, as well as some initial calibration.

Chapter 2

Theory

2.1 Electromagnetically Induced Transparency

EIT is a phenomenon that occurs when an atom is exposed to two electromagnetic (EM) fields, forming a Λ configuration (Fig. 2.1). The EM fields can be tuned such that the difference in frequencies between the two fields matches the frequency difference between the ground levels of an atom, or

$$\delta = (\omega_2 - \omega_1) - \omega_{bc} = 0 \tag{2.1}$$

Where ω_2 and ω_1 are the oscillating frequencies of the EM fields, ω_{bc} is the difference between the ground levels of the atoms, and δ is the two-photon detuning. When δ is 0, the atom decays after excitation into either the dark state (Eq. 2.2) or the bright state.

$$|D\rangle = \frac{1}{\sqrt{(\Omega_1^2 + \Omega_2^2)}}(\Omega_1|b> - \Omega_2|c> e^{\delta ixt}) \tag{2.2}$$

If the atom enters the dark sate $|D\rangle$, which is a superposition of the two ground states, it will become trapped in $|D\rangle$ and will not be excited. If the atom enters the bright state, which is orthogonal to the dark state, it will continue to be excited until it decays into the dark state. This phenomenon is known as Coherent Population Trapping (CPT), as the atom becomes "trapped" in a superposition of the ground states [5].

If a large number of identical Rb atoms are exposed the same two EM fields, they will all enter identical dark states. Thus, if one of the fields' frequency is swept while the other's frequency remains constant a "transparent" peak is created that is narrow compared to the width of an absorption resonance (Fig 2.1 b). As the width of the EIT resonance is inversely proportional to the lifetime of $|D\rangle$, the peak width can be further improved by preventing atoms from decohering (such as when they hit the walls of a vapor cell).

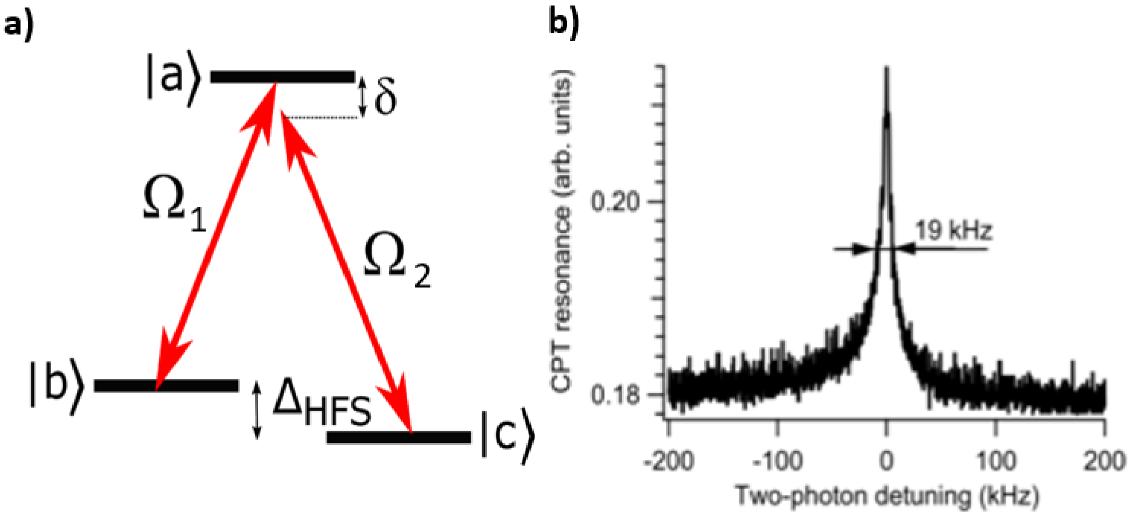

Figure 2.1: (a) Example of a three-level Λ configuration. (b) An EIT resonance. Modified from Ref [5]

2.2 Atomic Energy Levels and the Zeeman Effect

When atoms are exposed to an external magnetic field, they will experience a splitting of their degenerate energy levels. This is phenomenon called the Zeeman Effect. The separation between these energy sub-levels is directly proportional with the strength of the applied magnetic field.

$$\Delta E = mg\mu_B B \tag{2.3}$$

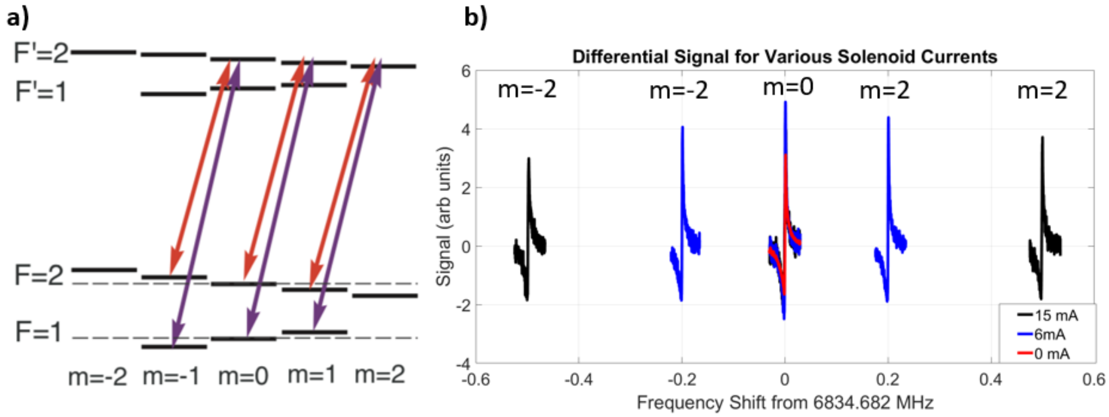

Figure 2.2: (a) Level diagram for D1 line of Rb showing the Zeeman sublevels. (b) Coherent population trapping resonance at zero magnetic field and for B $= 16\mu$T, B$=35\mu$T. Modified from Ref [5]

Where ΔE is the splitting of resonances, g is the gyromagnetic ratio, (g=2.0023193), m is the spin, $\mu_B = 5.788 \cdot 10^5 eV/T$ is the Bohr Magnetron, and B is the magnetic field[8]. Figure 2.2a shows the Zeeman sublevels of the D_1 line of Rb, figure 2.2b compares the EIT resonance of an Rb vapor that is exposed to a magnetic field of 0, 14, and 35 μT. The resonance shrinks and splits into three resonances (one central magnetically-insensitive resonance and two side magnetically sensitive resonances). In some cases we see multiple resonances on either side of the magnetically insensitive resonance, denoted ±m, ±2m, etc. The conversion factor for resonance separation to magnetic field strength is 700KHz/Gauss for m=±1 for ^{87}Rb [8].

2.3 Benefits of the dual-rail configuration

Our experiment uses two identical laser beams propagating through the Rb cell a set distance apart, or a dual-rail configuration. After the cell, the beams are measured by a balanced photodetecor (BPD) which can be operated in either single channel or differential mode. The BPD's signal is then sent to a lock-in amplifier. We use the

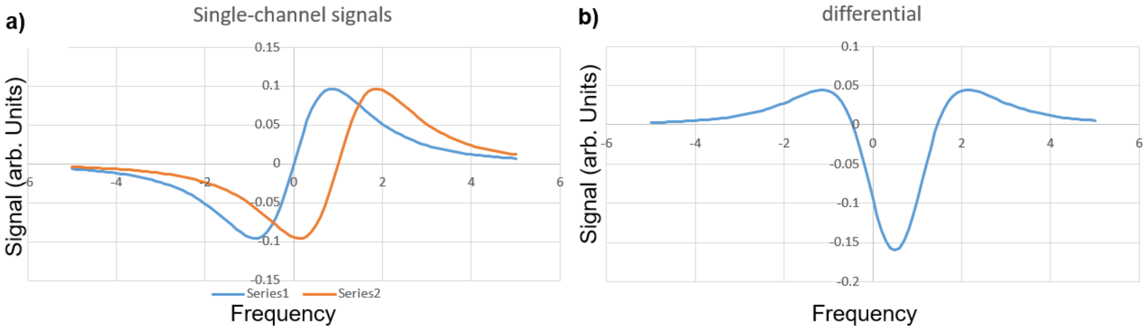

Figure 2.3: (a) Simulated single-channel signals with a slight offset, (b) resulting differential signal

differential signal for gradient measurement, as it reduces common noise and increases our sensitivity. Without a magnetic gradient, the frequency splitting of both beams will be symmetric, and the differential signal will be a flat line. With just the slightest gradient, however, the offset between the shifting creates a differential signal as shown in the simulated data of Fig 2.3. Using a balanced photodiode rather than subtracting

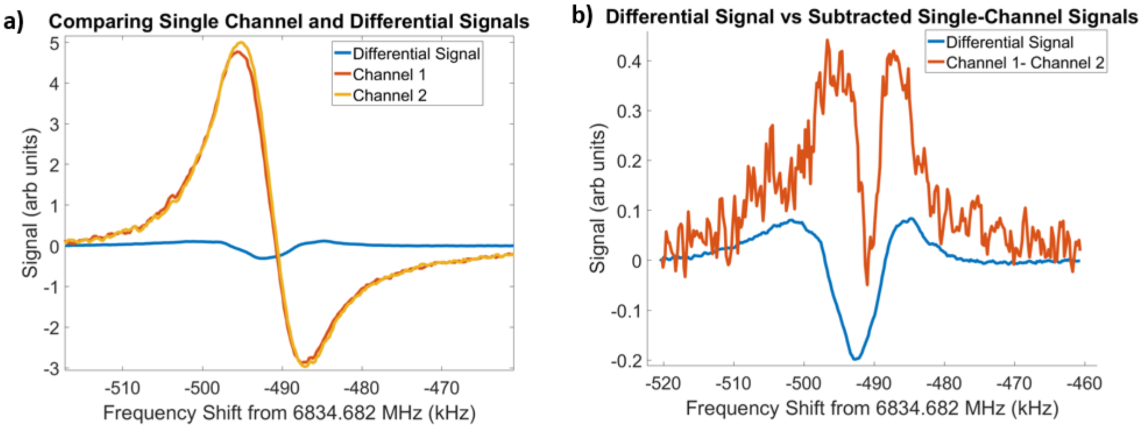

Figure 2.4: (a)The channel 1, channel 2, and differential signals of the m=-2 resonance. (b) Comparison of subtracting individual channels recorded separately vs the differential signal

two separately acquired individual single channel signals also reduces common noise, as demonstrated in Fig 2.4. Recording the height and frequency position of the differential signal will allow us to measuring the difference in magnetic field between the two beams, and thus the value of the gradient.

Chapter 3

Methods

3.1 Experimental Design

Figure 3.1 shows our experimental setup. A vertical cavity surface-emitting diode laser (VSCEL) operating at the Rb D1 line with a wavelength of 794.68 nm creates the two optical fields needed to achieve EIT. The VSCEL is current-modulated at the frequency of the ^{87}Rb ground state hyperfine splitting $\Delta_{HFS} \approx 6.834$ GHz. The dichroic atomic vapor laser lock (DAVLL) locks the laser to the correct frequency. A detailed description of the VCSEL current modulation and DAVLL arrangements can be found in Ref. [12]

After passing through the optical diode (OD), the VSCEL output was split into two beams using a Wallaston prism before propagating through a cell of Rb vapor. Each beam contains the two EM fields necessary to achieve EIT, and the beams are separated by 0.4 cm in the cell. The cell is a Pyrex cylinder (length 10 mm, diameter 22 mm) of Rb (liquid and saturated vapor) and 5 Torr Ne, heated to 57 ^{o}C. The Ne is a buffer gas which allows the atoms to propagate for longer times without colliding with the cell walls and decohereing, resulting in narrower resonances. The cell is surrounded by magnetic shielding, a solenoid, and gradient coils.

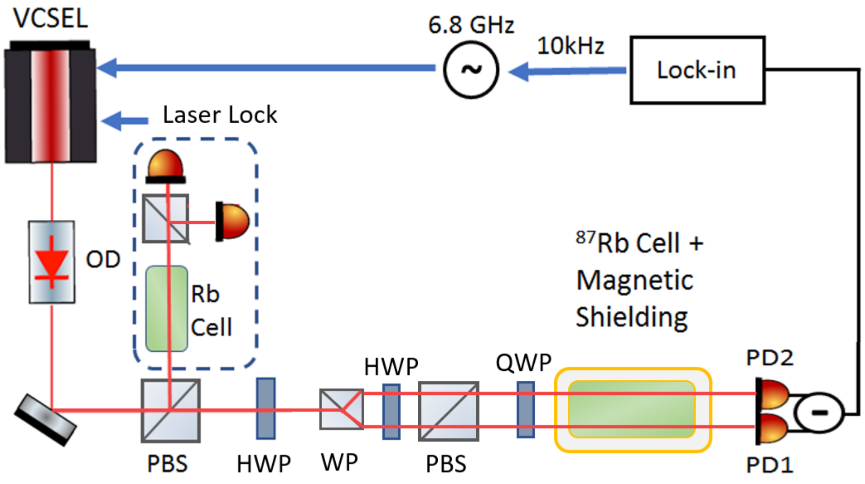

Figure 3.1: Setup schematic for differential detection.PBS=polarizing beam splitter, HWP=half wave plate, QWP=quarter wave plate WP= Wollaston Prism, PD=photodiode.

After the Rb cell two identical photodiodes (PD1 and PD2) detect the transmitter light intensities of both beams. When a gradient is applied, the beams will be passing through regions of slightly different magnetic field magnitude, thus the atoms they excite will have slightly different splitting due to the Zeeman effect (Eq 2.3). The photodiodes can be operated in either a single channel or differential mode. The benefits of using the differential signal are discussed in section 2.3. The photodiode signal is then sent to a lock-in amplifier. As the lock-in amplifier essentially takes the derivative of the input signal, the amplifier output signal shown in Fig 3.2b is sharper than the raw EIT transmission resonance in 3.2a.

3.2 Magnetic Field Generation

We can expose the ^{87}Rb vapor to a constant longitudinal magnetic field using a solenoid (Fig 3.3a), creating the necessary Earth-like magnetic field. The magnetic

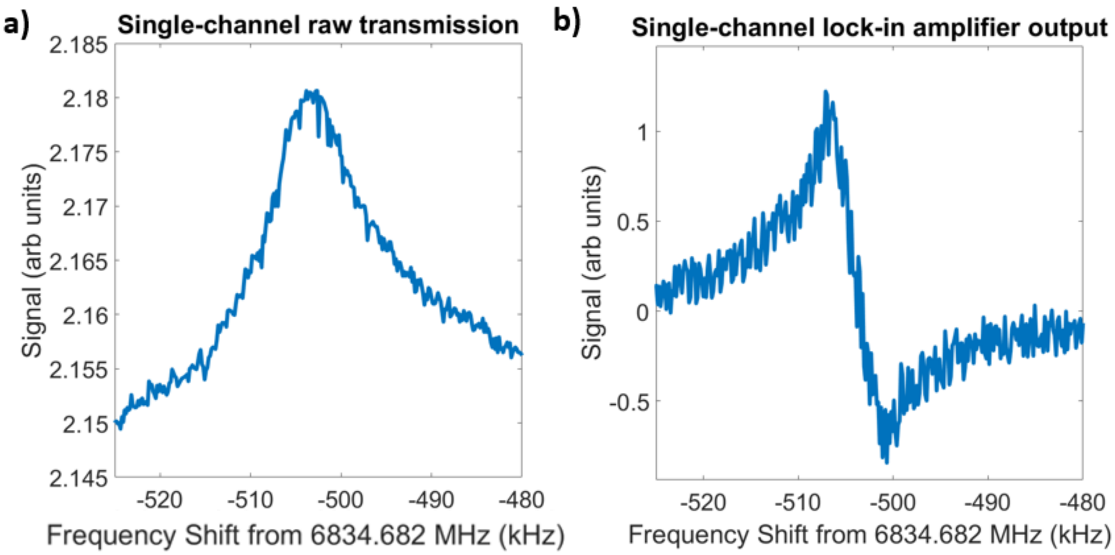

Figure 3.2: (a) Raw EIT single-channel transmission peak (b) EIT single-channel transmission peak after processing of the lock-in amplifier.

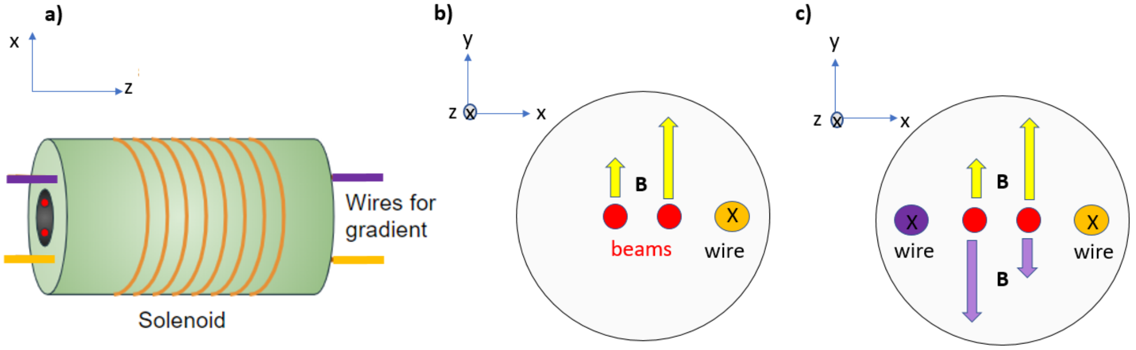

Figure 3.3: Methods for generating magnetic fields around the R^{87} cell (a) A constant longitudinal magnetic field is created by a solenoid. (b) the single-wire gradient configuration. (c) The two-wire gradient configuration.

field inside a solenoid is described by

$$B = \mu_o n I \tag{3.1}$$

where **B** is magnetic field, μ_o is the vacuum permeability constant, n is the number of loops of wire per unit length in the solenoid, and I is the current in the solenoid.

We have used two methods to generate the magnetic gradient. In the early stages

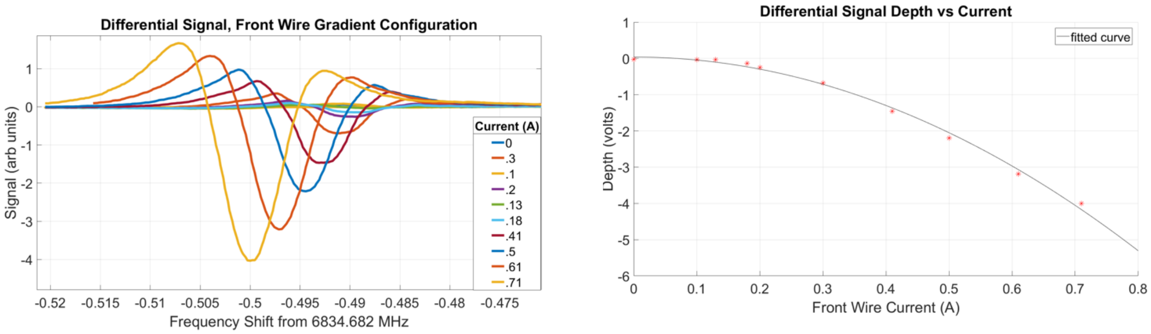

Figure 3.4: (a) Differential signal for various gradient currents (b) Analyzing signal size (depth) vs current.

of our experiment, we used two current-carrying straight wires running parallel to the laser beams to create a magnetic gradient, in either the two-wire or single-wire configuration. The single-wire configuration creates a magnetic field that is proportional to current I and inversely proportional to distance from the wire (r):

$$B = \frac{\mu_0 I}{2\pi r} \tag{3.2}$$

Thus in the single wire configuration a magnetic gradient is achieved, as one beam will propagate through a larger magnetic field than the other beam (Fig 3.3b). For the two-wire configuration, each wire produces magnetic fields of the same magnitude, but in opposite directions (Fig 3.3c). Thus, the magnetic fields at both beams are of opposite signs but similar magnitudes.

While the straight-wire method creates a magnetic gradient that is useful for early configurations of our setup, it also poses a problem: the splitting due to the combined gradient and solenoid fields is quadratically dependent on current in the single wire (Fig 3.4). This is because the solenoid produces a magnetic field in the z direction (in the direction of beam propagation), while the gradient wire produces a magnetic field in the y direction. Thus, the magnitude of the total magnetic field is described as follows.

$$B_{total} = \sqrt{B_{gradient}^2 + B_{solenoid}^2} \tag{3.3}$$

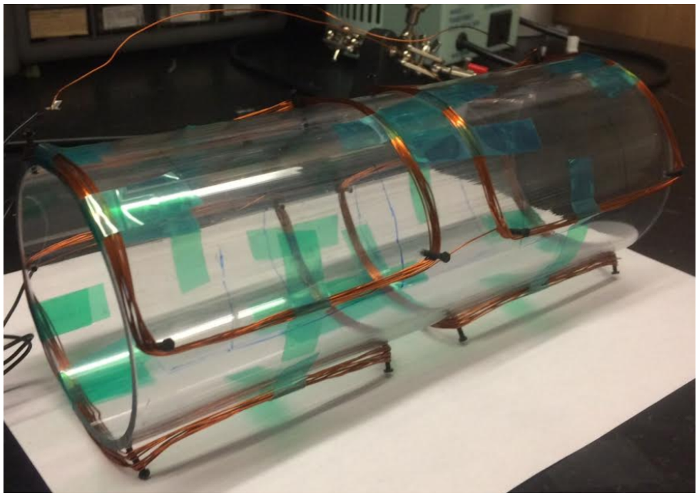

Figure 3.5: Gradient coil. The cell of ^{87}Rb vapor will be suspended inside the gradient coil, which in turn is inside the solenoid.

As $B_{solenoid}$ is much greater than $B_{gradient}$, this can be approximated using a Taylor expansion. Then from Eq. 3.2 we find that the total magnetic field is proportional to I^2 plus a constant solenoid field.

We are interested in measuring both constant gradients and gradients that change periodically (referred to as AC gradients). For constant gradients, we supplied a constant voltage to the coil and swept the two-photon detuning of the laser. By recording the position and height of the differential lock-in output (Fig 3.4), we can measure the magnitude of the constant gradient. For AC gradients, we kept the laser at one frequency and alternated the gradient by applying a sine wave to the gradient coil using a function generator. The amplitude of the sine wave was proportional to the magnitude of the magnetic gradient. In the differential configuration we then recorded the lock-in amplifier output over 200 seconds and mapped the data into Fourier space (Fig 5.2). The amplitude of the peak at sine wave's frequency is linearly proportional to the amplitude of the gradient, thus it can be analyzed to measure the gradient.

3.3 Magnetic Field Calibration

We calibrated the solenoid and gradient coil by measuring the frequency shift of the resonances versus current and using the conversion factor 1.4MHz/Tesla (the extra factor of two comes from the fact that we are looking at the Δm=2 resonance). Calibration of the two-wire gradient configuration can be found in Appendix A.

3.3.1 Solenoid Calibration

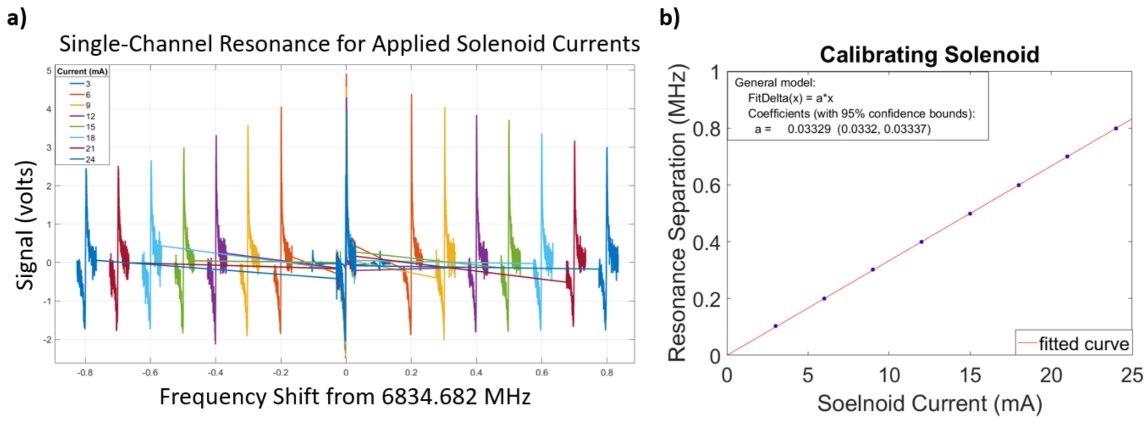

Figure 3.6: Calibrating the solenoid of the second cell. (a) Resonance width vs solenoid current for Δm=0,2 (b)Plotting single channel resonance position versus current.

We calibrated the solenoid by measuring the frequency shift of the each single-channel resonance versus current supplied to the solenoid. Figure 3.6 confirms the linear dependence expected from Eq. 3.1. For this calibration, there are no applied gradient fields. We took a linear fit of the EIT resonance shifting vs current (Fig 3.6) and found the following equation.

$$\Delta f[MHz] = 0.03329 \cdot I[mA] \tag{3.4}$$

Where Δf is the Zeeman splitting and I is applied current. Using the conversion factor, we then found the magnetic field produced by the solenoid.

$$|B|[T] = 2.377 \cdot 10^{-5} \cdot I[mA] \tag{3.4}$$

Where B is magnetic field and I is current in mA.

3.3.2 Calibrating Single Wire Gradient

We calibrated the single-wire gradient using only the front wire (Fig 3.7) with a constant magnetic field applied using the solenoid. As shown in Eq.3.3 and Eq.**??**, we expect the splitting due to the combined gradient and solenoid fields to be quadratically dependent on the current in the single wire.

We measured the m=-2 single channel resonance position for various applied currents, then used a quadratic fit to find the following equations (Fig 3.7).

$$\begin{array}{rl}
\text{Channel 1:} & B = 0.0165[T] \cdot I^2 + 0.351[\text{A}^2] \\
\text{Channel 2:} & B = 0.0116[T] \cdot I^2 + 0.351[\text{A}^2] \\
\text{Gradient:} & \frac{\Delta B}{\Delta x}[\frac{T}{cm}] = 0.1225 I^2[\text{A}^2]
\end{array}$$

Where B is the magnetic field magnetic field in Tesla and I is current in A. $\frac{\Delta B}{\Delta X}$ is in Tesla/cm and is calculated using the beam separation 0.4 cm. This process also demonstrated that the depth of the differential signal is quadratically dependent on the gradient.

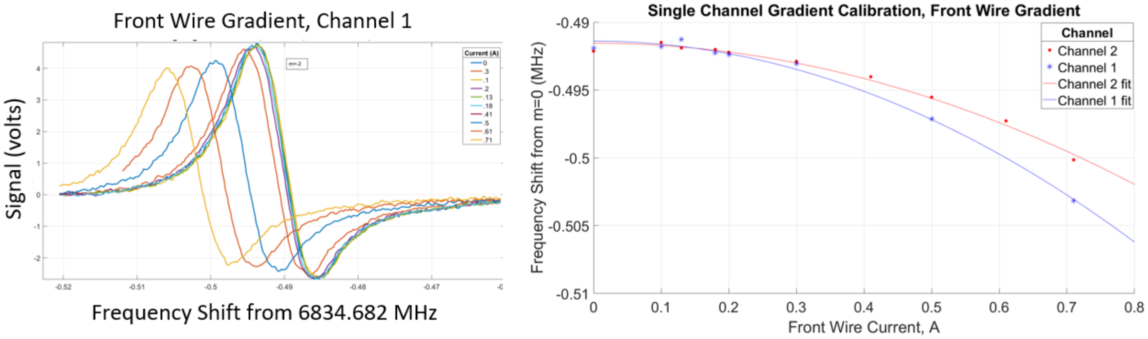

Figure 3.7: Front wire gradient calibration. (a) Single-channel signal for various currents. (b) Single-channel splitting vs current

3.3.3 Gradient Coil Calibration

We calibrated the gradient coil by supplying a constant voltage to the solenoid and measuring the frequency shift of the each single-channel versus current. Using the conversion factor of 1.4MHz/Tesla and dividing by the separation between the two beams (0.4 cm), we then found the gradient produced by the coil based on the supplied function generator offset (Fig 3.8).

$$\frac{\Delta B}{\Delta X} = 3 \cdot 10^{-7} \cdot V \tag{3.4}$$

Where $\frac{\Delta B}{\Delta X}$ is the gradient in T/cm and V is the offset in volts.

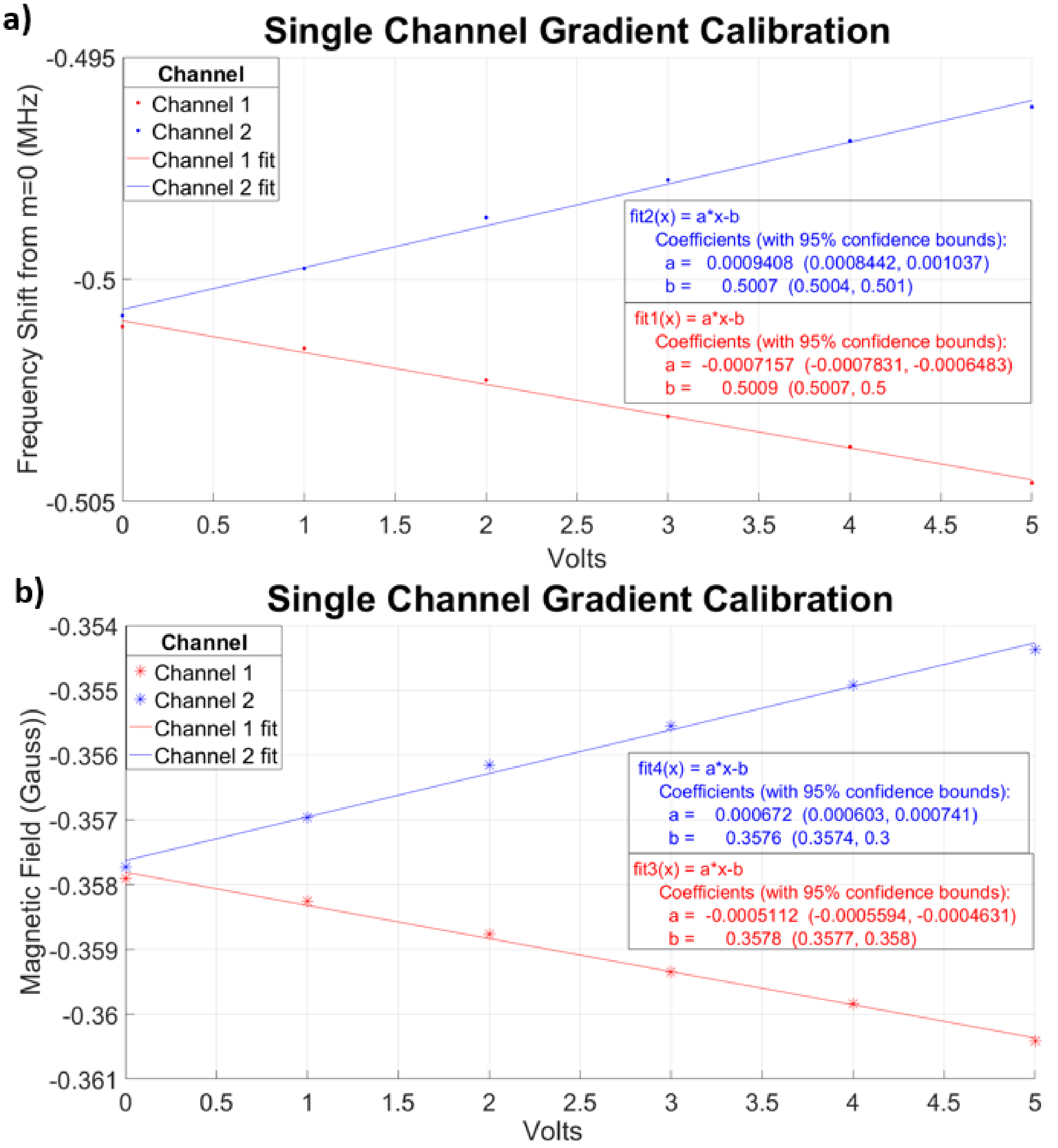

Figure 3.8: Linear gradient coil calibration. (a)Frequency separation vs voltage applied to gradient coil. (b) Magnetic field vs voltage applied to gradient coil.

Chapter 4

Constant Gradients

For constant gradients, we applied a constant voltage to the coil and swept the two-photon detuning of the laser. By recording the position and height of the differential lock-in output (Fig 3.4), we can measure the magnitude of the constant gradient. We took measurements using both the straight-wire gradient coil and the linear gradient coil.

4.1 Straight-wire Gradient Measurement

With a constant magnetic field of 35 μT produced by the solenoid, we applied a gradient field using the straight current-carrying wire and recorded the m=-2 resonance differential signal. We plotted the size of the differential signal vs current (which in turn gives us magnetic gradient), and found a quadratic dependence for currents of 0.1 to 0.8 A (Fig. 3.4). This is expected, as discussed in chapter 3.2. We then explored the sensitivity of using the differential resonance size to measure magnetic gradients. Figure 4.1a shows the differential resonance with applied currents of 0 to 0.22 A. Surprisingly, the differential signal is non-zero when zero gradients are applied. This is due to the Transit-Ramsey EIT (TREIT) effect, which is discussed in Appendix B. Visually analyzing Figure 4.1b, one can see that the the resonance depth begins to plateau around 0.12 A, thus we concluded that our gradient sensitivity for

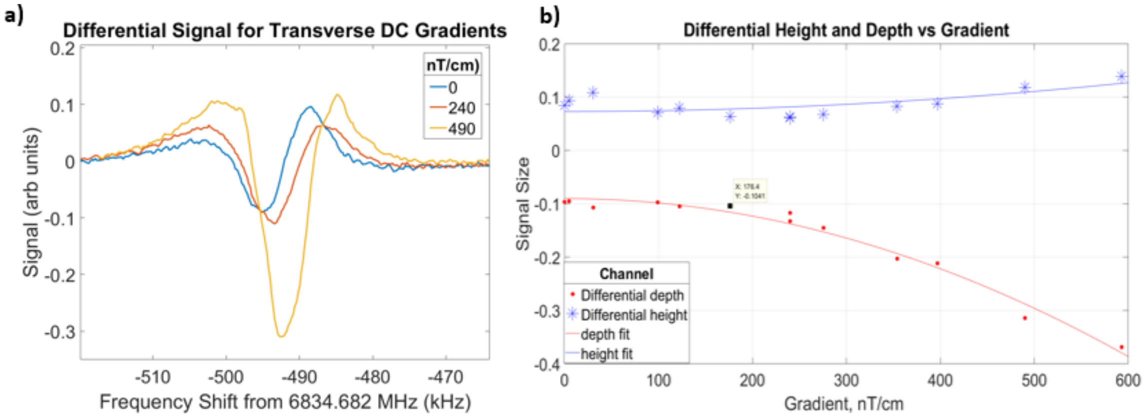

Figure 4.1: (a) Differential Signal for small currents (b) Analyzing signal height and depth vs current.

straight-wire gradients is about 170 nT/cm.

4.2 Linear Gradient Coil Measurements

We repeated the steps in section 4.1 using the linear gradient coil. The negative gradients in Fig 4.2 correspond to a negative voltage applied to the gradient coil. By dividing the standard deviation of the signal height at zero gradients by the slope of the linear fit, we estimate our sensitivity to be 7 nT/cm. As expected, the linear gradient coil measurements produced a higher sensitivity than the straight wire gradients.

We also attempted to increase our sensitivity by subtracting the zero-gradient TREIT signal (Fig4.2b), however due to laser drift the position of the resonance shifted slightly during measurement, which interfered with subtracting as the various differential signals were no aligned perfectly. Plotting differential signal height versus gradient for the zero-gradient subtracted signal and taking a linear fit gave a larger error than the non-subtracted differential signal, however the subtraction technique could be explored further.

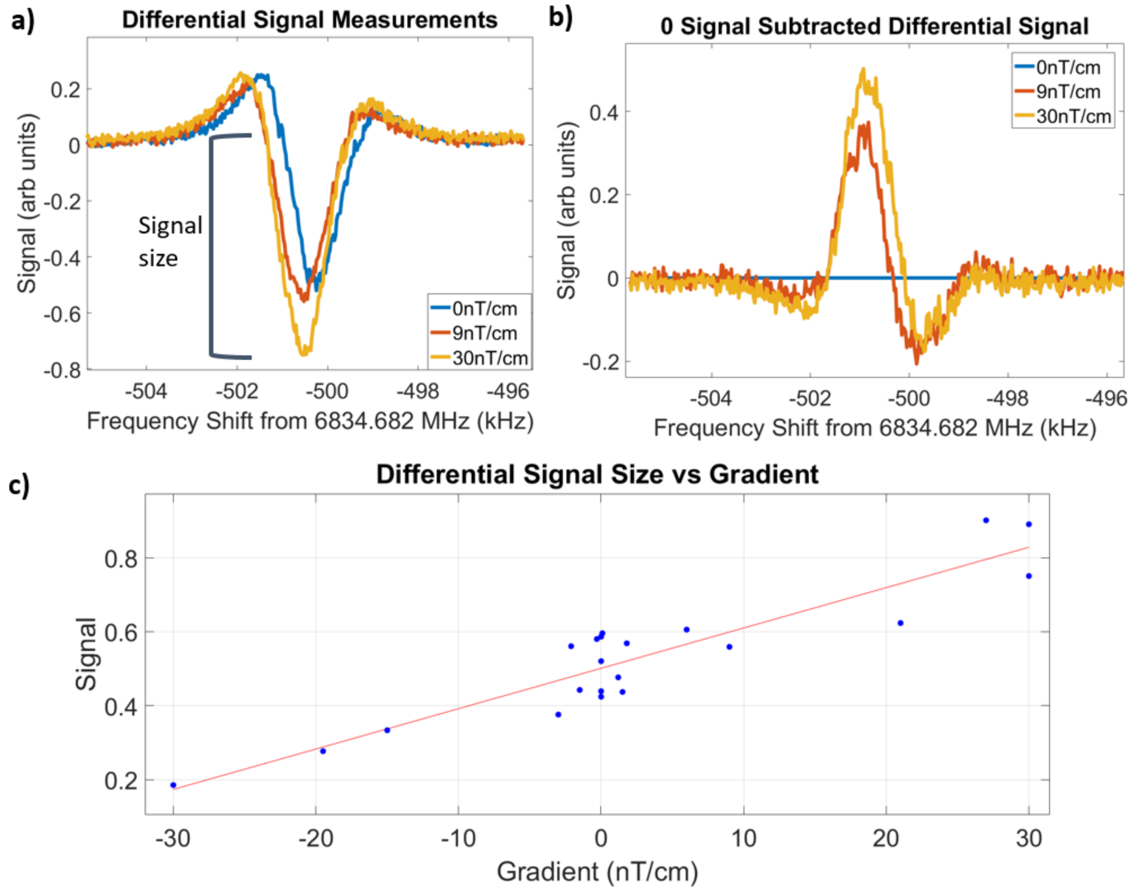

Figure 4.2: (a)Differential signal of the Δ m=-2 resonance with a 35μT Earth-like magnetic field and 0, 9, and 30nT/cm gradients applied. (b) Subtracting the 0-gradient signal from differential signal. (c) Differential signal height vs gradient.

Chapter 5

AC Gradients

While the constant magnetic gradient measurements were made by sweeping the two-photon detuning frequency and applying a constant current to the gradient coil, for AC magnetic field measurements we fixed the laser modulation frequency at 6.834GHz and used a function generator to apply a 1 Hz sine wave to the coil. As the size of the differential signal grows proportionally with magnetic field magnitude, the amplitude of the sine wave will be proportional to the lock-in amplifier output. We chose 1 Hz as our frequency because it is approximately the frequency of a resting human heart beat.

Looking at the lock-in amplifier output over many periods of the gradient sine

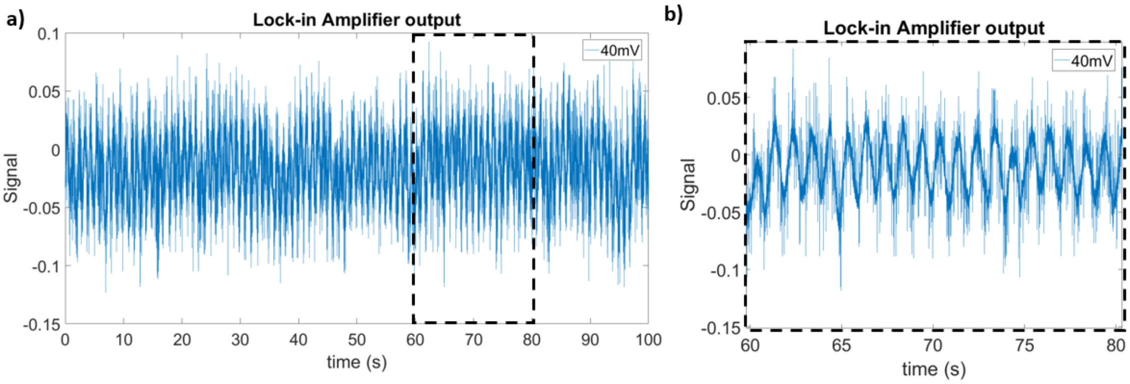

Figure 5.1: a) Lock-in amplifier output with a 1Hz sine wave with an amplitude of 40 mV applied to the linear gradient coil. b) Zoom in on 60-80 second range to see short term oscillation.

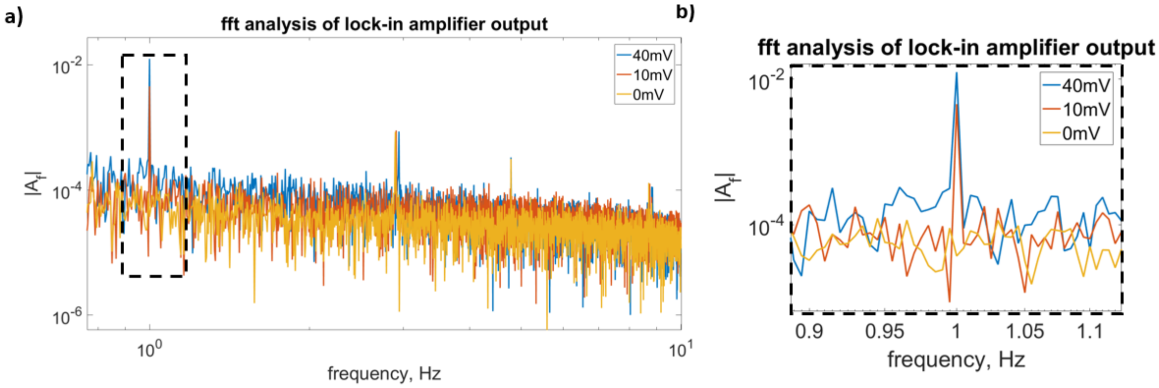

Figure 5.2: a) Fourier transform of lock-in amplifier output with 1Hz sine wave with an amplitude of 0, 10, and 40 mV applied to the linear gradient coil. Note peak at 1 Hz and 60Hz. b) Zoom in on 1Hz peak, which shows dependence on sine wave amplitude.

wave, a significant amount of noise and drifting is apparent (Fig 5.1). Therefore, instead of using the raw lock-in output to measure gradients, we took a Fourier transform of the data. Figure 5.2a displays the Fourier transform over a range of about 1-10 Hz in which a few peaks are present, suggesting a number of periodic noise sources. We are interested in analyzing the 1Hz peak, as its height is proportional to the amplitude of the magnetic field gradients. Before making the AC gradient measurements, however, we made sure to optimize the lock-in amplifier settings and the laser power in order to maximize our sensitivity.

5.1 Lock-in Amplifier Optimization

Focusing on the AC gradient configuration, we optimized the time constant, modulation frequency, modulation amplitude, and gain of our lock-in amplifier.

One way to understand the noise of a signal over many periods is by looking at it's Allan Variance. The Alan variance, or two-sample variance, is used to describe frequency stability in atomic clocks. We used this method to explore the lock-in output behavior over time, and specifically to optimize the time constant (τ_{mod}) of the lock-in amplifier. Figure 5.3 shows the Allan variance $\sigma_y(\tau)$ vs time for different time constants. The lower the Allan variance, the more stable the frequency. Thus, 10 ms is the optimal time constant.

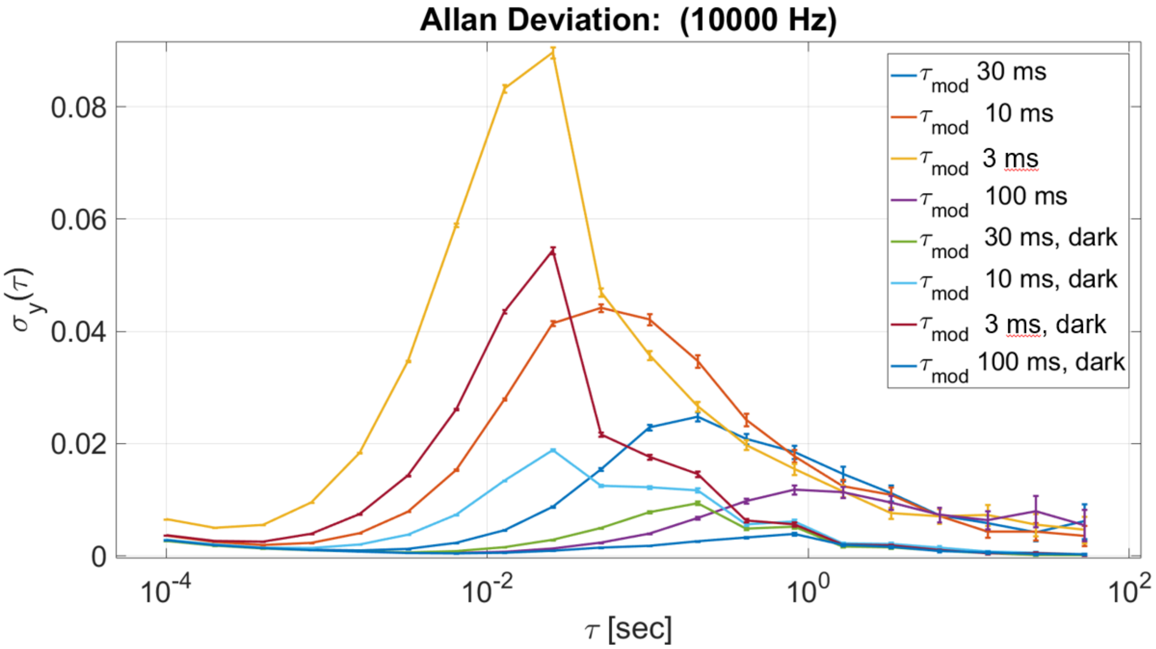

Figure 5.3: Alan variance vs time for a variety of time constants (τ_{mod}). "Dark" signifies that the laser beams were blocked while taking that data.

We optimized modulation frequency by recording 200 seconds of the lock-in amplifier output for various modulation frequencies with and without magnetic gradients. We took the Fourier transform of the gradient data (gradient frequency=1Hz) and measured the height of the 1Hz peak (5.4a). We used the data without an applied gradient to measure the noise level by taking the average around the 1Hz peak (5.4b). Plotting the signal-to-noise ratio vs modulation frequency, we concluded that the optimal modulation frequency is around 17kHz. This frequency we used for all later measurements.

The methods for optimizing modulation amplitude and gain were similar to op-

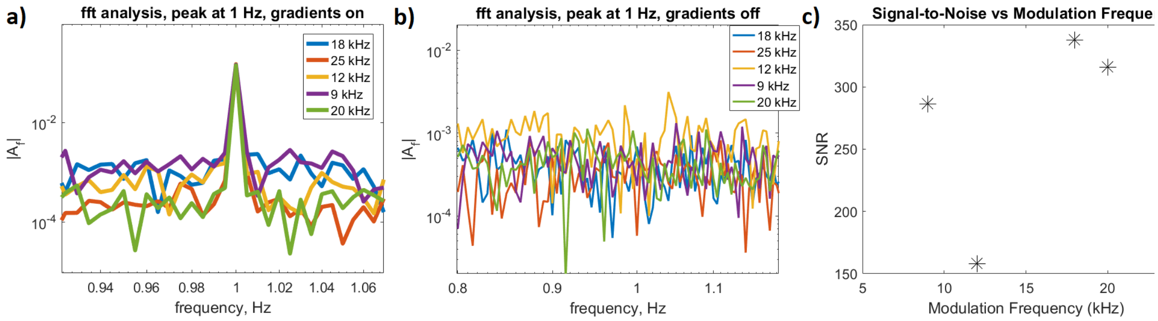

Figure 5.4: Optimizing Modulation Frequency. a) Gradients on, 1 Hz peak for various applied modulation frequencies. b) Gradients off, noise near 1Hz for various modulation frequencies. c) Signal-to-noise ratio vs modulation frequency. Optimal modulation frequency: 17kHz

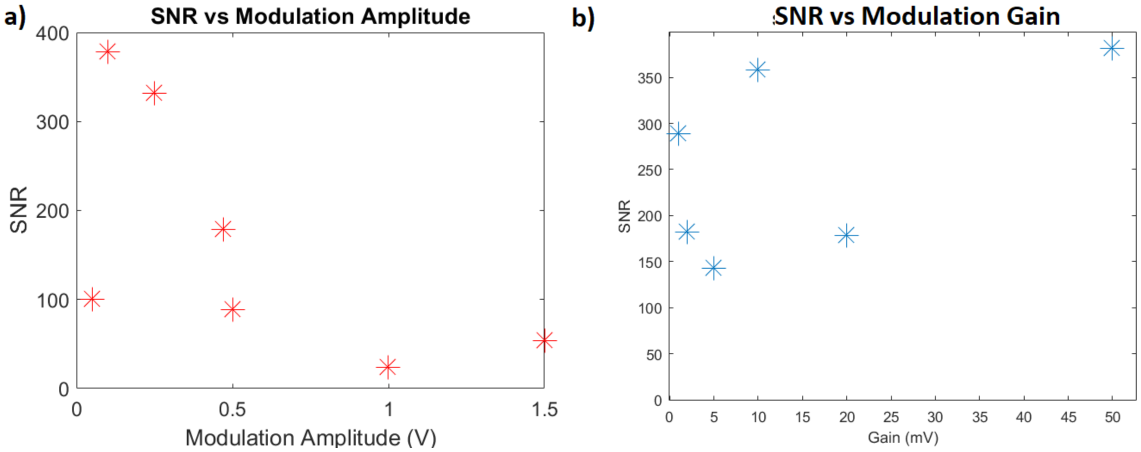

Figure 5.5: (a) Signal-to-noise ratio vs modulation amplitude. Optimal modulation amplitude: 0.22V (b) Signal-to-noise ratio vs modulation gain. Optimal modulation gain: 10mV

timizing the modulation frequency. Figures 5.5a and 5.5b show the Signal-to-noise ratio versus modulation amplitude and gain, respectively. We concluded that the optimal modulation amplitude is 0.22V, and the optimal gain is 10mV.

To summarize, Table 5.1 shows all lock-in amplifier settings that we optimized.

Parameter	Optimal Setting
Time constant	10ms
Modulation Frequency	17kHz
Modulation Amplitude	0.22V
Modulation Sensitivity	10mV

Table 5.1: Optimized lock-in settings

5.2 Power Optimization

Similarly to the lock-in amplifier optimization, we optimized the laser power by trying to maximize the 1Hz peak and minimize noise of the Fourier transformed data. Laser power we controlled using ND filters. Figure 5.6 shows the Signal-to-noise ratio versus power. We concluded that the optimal laser power is around $35\mu W$

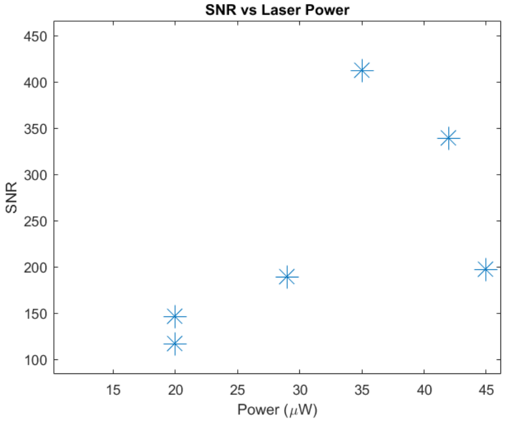

Figure 5.6: Signal-to-noise ratio versus laser beam power

5.3 Measuring AC Gradients

With the optimized settings detailed above, we then moved on to measuring the sensitivity of our gradiometer to AC gradients. To do this, we applied a voltage to the gradient coil and measured the height of the 1Hz peak (Fig5.7a). Using the calibration in Chapter 3 and taking a linear fit, we were then able to find the relationship of peak height to magnetic gradient.

While our function generator had a limit of .01 V (1 nT/cm), we could estimate our sensitivity by taking the average of the lock-in output around 1 Hz with 0 gradients (our "noise floor") and finding where our fit crosses that limit. Thus we can see from figure 5.7 that our sensitivity for AC gradients is 50 pT/cm.

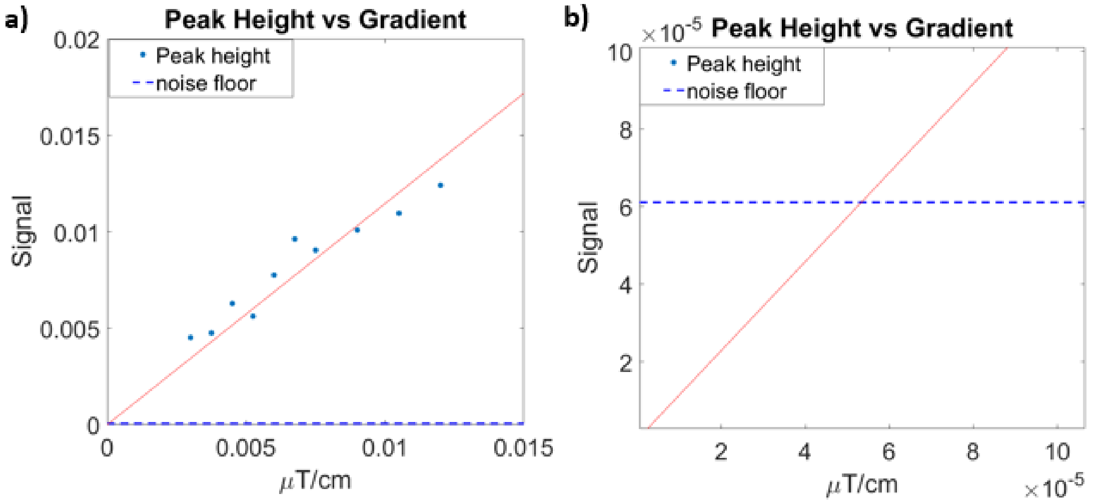

Figure 5.7: (a) Height of the lock-in amplifier's Fourier-transform 1Hz peak vs gradient. Noise floor indicates minimum peak size that can be discerned above noise. (b) Zooming in on crossing of noise floor gives the sensitivity, 50μT/cm

Chapter 6

Conclusions and Future Work

Measuring small magnetic fields without using shielding or multiple magnetometers has applications in geology, defence, medicine, and beyond. We have demonstrated a technique that can measure a minimum DC gradient of 7 nT/cm and a minimum AC magnetic field of 50 pT/cm in the presence of an Earth-like magnetic field. For our AC gradient measurements, we have achieved the desired sensitivity for this technique to be used in developing equipment for magnetocardiology.

Our method improves on other magnetometers in terms of need for magnetic shielding and frequency of gradients. The optically-pumped magnetic gradiometer described in Ref [9], for example, achieves a sensitivity 10 fT/Hz$^{\frac{1}{2}}$ at frequencies above 20Hz, however our technique measures AC gradients produced using a 1Hz sine wave, which is the frequency of a resting human heart beat and thus is more applicable in magnetocardiology [9]. SQUID magnetometers, one the most frequently used devices in detecting biomagnetic signals, can detect magnetic fields three orders of magnitude smaller than our technique, however this technique requires a cyrogenic cooling and magnetic sheidling. These restrictions limit the use of SQUID magnetometers in medicine, as hospitals would require a dedicated magnetically-shielded room for measuring magnetocardiograms. Furthermore, our method is compact as its use of a dual-rail configuration only requires one Rb cell. For example the Grad-

01-100L single access gradient sensor by Barington Instruments, which achieves a sensitivity of 0.03nT/m, uses two magnetometers separated by a meter, however we can reach a similar order of magnitude using only one magnetometer. [10].

Future work for this project will involve producing and measuring gradients that more closely imitate the magnetic fields produced by a human heart. To be used in creating a magneotocardiogram, the magnetometer will have to detect AC gradients with frequency in the 1-100 Hz range and amplitude of 10-100 pT [3]

Appendix A

6.1 Atomic Density Calibration

The density of Rb vapor is determined by the temperature of the cell, with a higher temperature resulting in a greater atomic density. We wanted to record this dependence and find an optimal cell temperature for data collection. To do this, we recorded the Rb absorption spectrum for a range of temperatures and from the shape of the spectrum calculated the atomic density using a fit function using the Atomic Density Matrix *Mathematica* package from Rochester scientific (Fig 6.1) [11].

Cell Temperature ^{o}C	Rb Density cm^-3
43	$6.610\times^{10}$
50	9.0×10^{10}
53	9.0×10^{10}
55	9.0×10^{10}
57	9.0×10^{10}

Table 6.1: Cell temperature vs ^{87}Rb density

Surprisingly, a cell temperature of 50^{o}C to 57^{o}C resulted in a constant Rb density. Although the fitting results are consistent withing a percent it is clear that more analysis of temperature dependence is needed. For simplicity we decided to use 57^{o}C with the knowledge that our Rb density is $9.0\cdot10^{10}$ atoms/cm^3, but this is likely an area of future optimization.

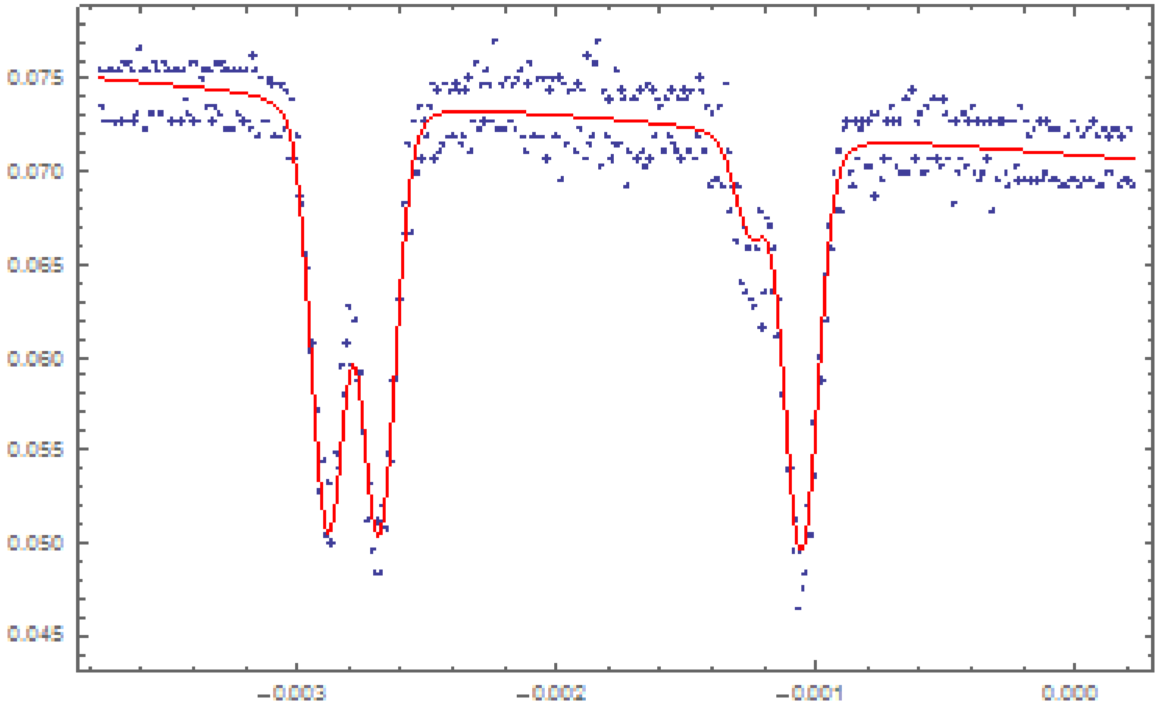

Figure 6.1: Example of ^{87}Rb Absorption Spectrum at 57 C

Appendix B

6.2 Transit Ramsey EIT resonances

This work used a cylindrical Pyrex cell (length 75mm, diameter 22mm) containing isotopically enriched ^{87}Rb vapor, heated to 44.5C. With our setup in configuration A (Fig 6.2a), we began exploring the differential signal produced when the Rb atoms are exposed to various applied magnetic fields with. It was during this exploration stage that we noticed an unusual feature in the differential signal when no magnetic fields were applied (Fig 6.2a). We expected the differential signal to be flat without an external applied magnetic field, so this none-zero feature indicated that our beams were somehow not identical. After attempting to reduce this feature by degaussing the cell, changing the mirrors, optimizing the cell position, and studying the power broadening of the two beams, we concluded that the imbalance was due to the path

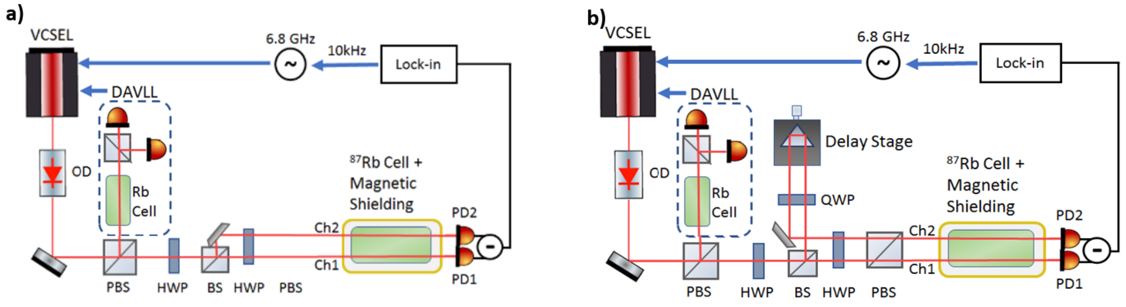
a)
VCSEL
6.8 GHz
10kHz
Lock-in
DAVLL
OD
Rb Cell
^{87}Rb Cell + Magnetic Shielding
Ch2
Ch1
PD2
PD1
PBS
HWP
BS
HWP
PBS
b)
VCSEL
6.8 GHz
10kHz
Lock-in
DAVLL
OD
Rb Cell
Delay Stage
QWP
^{87}Rb Cell + Magnetic Shielding
Ch2
Ch1
PD2
PD1
PBS
HWP
BS
HWP
PBS

Figure 6.2: Setup schematic for differential detection. For single channel measurement one of the channels is blocked before the cell. (a) Beam is split using beam splitter and mirror. (b) Setup with delay stage for TREIT work.

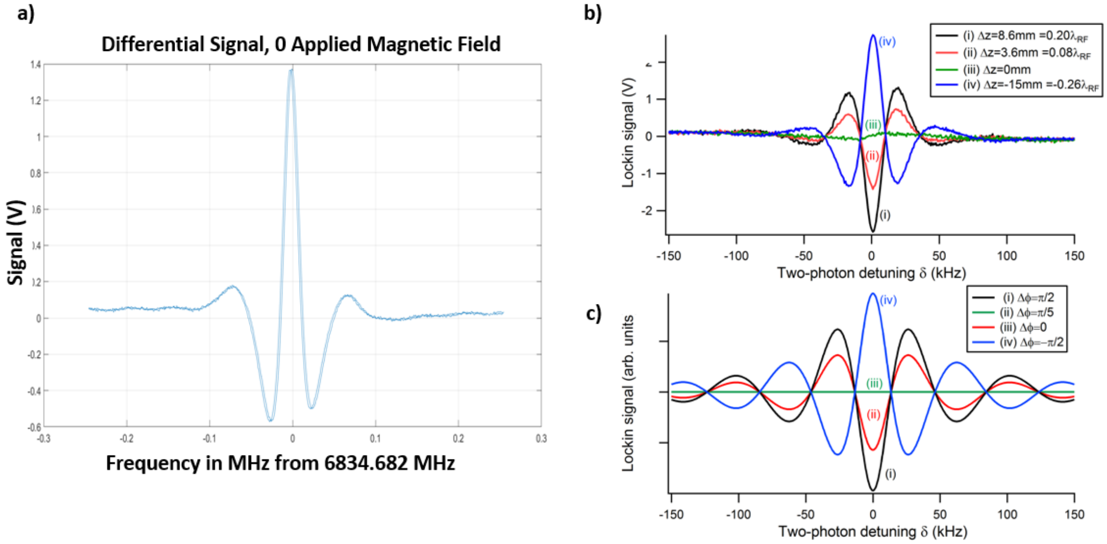

Figure 6.3: (a) Non-zero differential signal with 0 applied magnetic fields (first observation of TREIT resonance)(b) The differential lock-in signals as a function of the two-photon detuning for different relative prism position. Laser power in each channel is 50 μ W. (c) Theoretical simulations of the lock-in readout of the differential TREIT. 6b and 6c modified from Ref [7]

difference between the two beams created when they are split before the cell (Fig 6.2a).

The path difference caused the two laser fields in each beam necessary to achieve EIT to become out of phase with each other(Fig 6.4b). Atoms that interact with both beams are excited twice, and therefore experience a phenomenon that replicates the original Ramsey experiment [13]. To further study this phenomenon, we added a delay line to our setup, which allowed us to control the path difference between the two beams (Figure 6.2b). By changing the manipulating the path difference, we expected to be able to change the shape of the TREIT resonance (Fig 6.2c).

By manipulating the path difference we were able to almost completely reduce the TREIT resonance (Fig 6.2b). We also discovered some benefits to an amplified TREIT resonance.The TREIT resonance is much narrower and has a higher signal-to-noise ratio than the single-channel EIT resonance (Fig6.4a,c). A detailed report

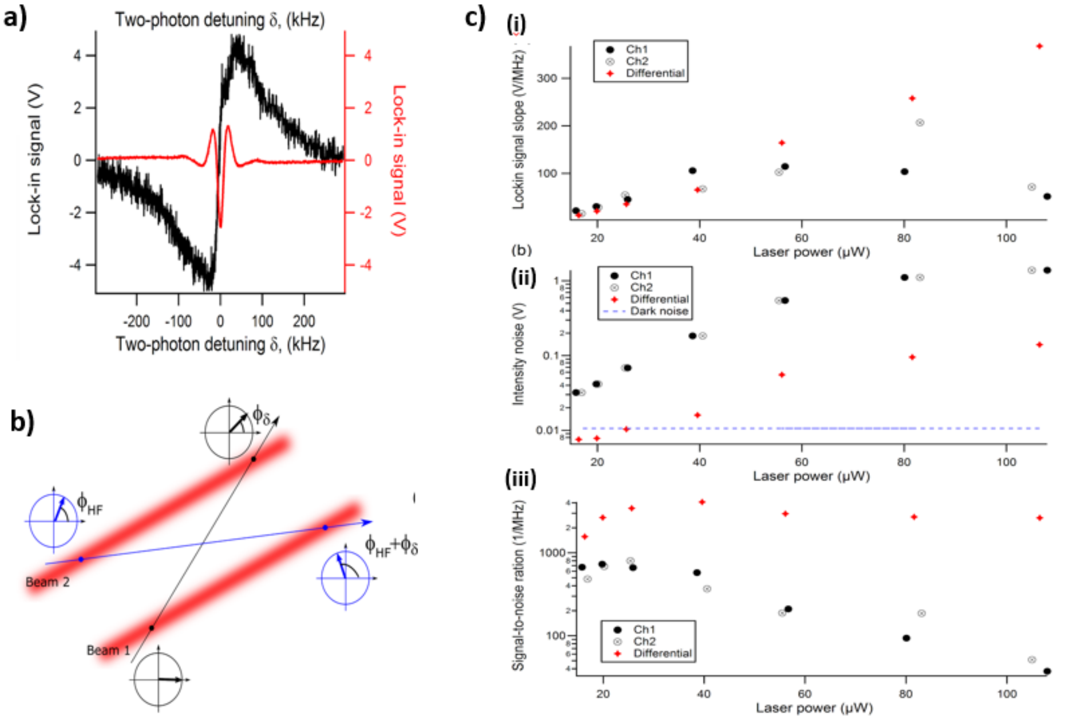

Figure 6.4: (a)Examples of the optical transmission for a single-channel EIT and for the intensity difference between the two channels. (b) Simplified geometry of the two-channel transient EIT setup. The arrows in the circles indicate the dark state phases of two atoms traveling symmetrically between the beams. For this illustration we set the phase between the two EIT optical fields to be zero in the first beam and ϕ HF $\neq 0$ for the second beam. In case of the non-zero two-photon detuning δ, the dark state phases of both atoms evolve by $\phi\delta = \delta \cdot \tau$ after τ transit time between the two beams, resulting in the difference in the optical response during the repeated interrogation. (c) (i) Slope of the error lock-in signal for each optical channel and for the differential signal at the corresponding zero-crossing detunings. (ii) lock-in noise measured at zero-crossing two-photon position. Horizontal line shows the dark electronic noise level. (iii) Signal-to-noise ratio (defined as slope of the error signal divided by the measure noise). For the differential measurements the average power between the two channel is used. Modified from Ref [7]

of our findings can be found in Ref [7]

Bibliography

[1] Cox, Kevin, "Vector Magnetometer Using Rb Vapor" (2011). *Undergraduate Honors Theses*. Paper 358.

[2] Romalis, Mike. "High Sensitivity Potassium Magnetometer." Princeton University. Accessed May 01, 2019. http://physics.princeton.edu/romalis/magnetometer/.

[3] Belfi, J., Bevilacqua, G., Biancalana, V., Cartaleva, S., Dancheva, Y., Moi, L. (2007). Cesium coherent population trapping magnetometer for cardiosignal detection in an unshielded environment. *Journal of the Optical Society of America B, 24(9), 2357.* doi:10.1364/josab.24.002357

[4] Bison, G., Wynands, R., Weis, A. (2003). A laser-pumped magnetometer for the mapping of human cardiomagnetic fields. *Applied Physics B: Lasers and Optics, 76(3), 325-328.* doi:10.1007/s00340-003-1120-z

[5] N. Belcher, E. E. Mikhailov, I. Novikova, Am. J. Phys. **77**, 988-998 (2009)

[6] Carlson, J. W. (1988). U.S. Patent No. 4,755,755. Washington, DC: U.S. Patent and Trademark Office.

[7] Ravn M. Jenkins, Eugeniy E. Mikhailov, and Irina Novikova, "Transit Ramsey EIT resonances in a Rb vacuum cell," J. Opt. Soc. Am. B 36, 890-895 (2019)

[8] S. A. Steck,*Rubidium 87 D Line Data*Theoretical Divdision (T-8), MS B285, Los Alamos National Labratory, (2003)

[9] Sheng, D., Perry, A., Kryzewski, S., Geller, S., Kitching, J., Knappe, S. (2017). A microfabricated optically-pumped magnetic gradiometer. *Applied Physics Letters, 110*(3). doi:10.1063/1.4974349

[10] Barington Instruments Limited. *Operation Manual for Grad-01-100L Single Axis Fluxgate Magnetic Gradiometer* Witney, Oxford, England

[11] Rochester, Simon. "Atomic Density Matrix." Rochester Scientific. Accessed May 01, 2019. http://rochesterscientific.com/ADM/.

[12] E. E. Mikhailov, T. Horrom, N. Belcher, and I. Novikova, *J. Opt. Soc. Am.* **B 27**, 417 (2010),

[13] N.F. Ramsey, Phys. Rev. V 78, 695,(1950)